Defects and Dopants in CaFeSi$_2$O$_6$: Classical and DFT Simulations

Navaratnarajah Kuganathan [1,2,*] and **Alexander Chroneos** [2]

[1]   Department of Materials, Imperial College London, London SW7 2AZ, UK
[2]   Faculty of Engineering, Environment and Computing, Coventry University, Priory Street, Coventry CV1 5FB, UK; ab8104@coventry.ac.uk
[*]   Correspondence: n.kuganathan@imperial.ac.uk or ad0636@coventry.ac.uk

Abstract: Calcium (Ca)-bearing minerals are of interest for the design of electrode materials required for rechargeable Ca-ion batteries. Here we use classical simulations to examine defect, dopant and transport properties of CaFeSi$_2$O$_6$. The formation of Ca-iron (Fe) anti-site defects is found to be the lowest energy process (0.42 eV/defect). The Oxygen and Calcium Frenkel energies are 2.87 eV/defect and 4.96 eV/defect respectively suggesting that these defects are not significant especially the Ca Frenkel. Reaction energy for the loss of CaO *via* CaO Schottky is 2.97 eV/defect suggesting that this process requires moderate temperature. Calculated activation energy of Ca-ion migration in this material is high (>4 eV), inferring very slow ionic conductivity. However, we suggest a strategy to introduce additional Ca^{2+} ions in the lattice by doping trivalent dopants on the Si site in order to enhance the capacity and ion diffusion and it is calculated that Al^{3+} is the favourable dopant for this process. Formation of Ca vacancies required for the CaO Schottky can be facilitated by doping of gallium (Ga) on the Fe site. The electronic structures of favourable dopants were calculated using density functional theory (DFT).

Keywords: CaFeSi$_2$O$_6$; defects; diffusion; dopants; DFT; classical simulation

1. Introduction

Over the last two decades, great progress has been made in the development of rechargeable lithium (Li)-ion batteries. However, there is a necessity to find alternatives to Li-ion batteries as energy demand increases rapidly with the world population. In this respect, sodium (Na) batteries are currently being considered mainly due to the high abundance of Na [1–4]. Batteries based on multivalent cations such as magnesium (Mg^{2+}) and zinc (Zn^{2+}) are also promising, as they can provide high energy density [5–9].

A Ca-ion battery is being currently considered as an alternative to Li-ion battery mainly due to the low cost associated with high abundance of Ca and high energy density [10]. However, Ca-ion diffusion is expected to be slow due to its larger ion size compared to that of Li. Furthermore, it is expected that there will be strong attractive or repulsive forces between migrating Ca ions and surrounding ions due to the double positive charge of Ca.

A variety of compounds such as garnets (e.g., Ca$_3$Fe$_2$Si$_3$O$_{12}$), pyroxenes (e.g., CaMnSi$_2$O$_6$), double carbonates (e.g., CaMg(CO$_3$)$_2$), marokites (e.g., CaMn$_2$O$_4$) have been tested as cathode materials for application in Ca-ion batteries experimentally or theoretically [11,12]. In a combined experimental and theoretical study on CaMn$_2$O$_4$ by Arryo-de Dompablo et al. [12], it was concluded that deinsertion of Ca ions from CaMn$_2$O$_4$ is hard, and this was further confirmed by the high activation energy (1.00 eV) calculated for the Ca-ion migration. In a DFT (Density Functional Theory) study by Torres et al. [11]

on pyroxene, garnet and double carbonate-based minerals, it was shown that deintercalation would provide high energy densities and Ca-ion diffusion in these materials would be slow.

"Hedenbergite" $CaFeSi_2O_6$ [13] is a silicon-based Ca-bearing mineral which is of great interest for designing electrode material as Si and Fe are safer, abundant and cheap. Furthermore, the great structural stability required during the intercalation is expected to be provided by strong Si–O bonds in SiO_4 units. Electrode materials based on $[SiO_4]^{4-}$ poly anion have been synthesized and their electrochemical activities tested for Li, Na and Mg ion batteries [14–16]. In addition, theoretical studies have also been explored on silicate-based materials to examine defects, diffusion and dopants [17–20].

Understanding the defect and diffusion properties of energy materials via computational modelling is an efficient complementary way for the design of promising energy devices. In many cases, computational studies have been successful in the determination of experimental crystal structures and ion migration pathways and prediction of promising isovalent and aliovalent dopants in many oxide materials [21–26]. In this work, we examine the intrinsic defect processes, Ca-ion diffusion pathways and promising doping strategies.

2. Computational Methods

Computational simulations were performed using classical simulation and DFT simulation. Classical simulations as implemented in the generalized used lattice program (GULP) [27,28] allowed the modelling of the energy minimized crystal structure with equilibrium lattice constants, calculation of the lowest energy defect process, identification of the promising dopants at different cation sites and the simulation of the Ca-ion diffusion pathways with the respective activation energies of migration. This method consists of two main ionic interactions, namely, long range (Coulombic) and short range (repulsive—Pauli—and attractive—van der Waals). Buckingham potentials were used to model short-range interactions. Point defects were modelled using Mott-Littleton method [29], as adopted in the GULP code. Core-shell model was applied to consider the polarization of ions in the lattice. In line with the previous studies [30], Ca-ion migration calculations were performed by following the method developed by Catlow et al. [31].

Electronic structures of the most favourable dopants were calculated using a plane wave DFT code VASP (Vienna ab initio simulation program) [32,33], which uses projected augmented wave (PAW) potentials [34] and plane wave basis sets. A plane wave basis set with a cut-off of 500 eV and Monkhorst pack [35] k-points ($4 \times 4 \times 4$) were used in all calculations. For defect modelling, a supercell containing 80 atoms was used. Exchange correlation was modelled using generalized gradient approximation (GGA) implemented by Perdew, Burke, and Ernzerhof (PBE) [36]. Both atomic positions and the cell parameters optimized using conjugate gradient algorithm [37]. Short range attractive interactions arising from dispersion were modelled using a semi-empirical scheme (DFT+D3) as implemented in the VASP code [38].

3. Results

3.1. Crystal Structure of CaFeSi₂O₆

$CaFeSi_2O_6$ is monoclinic with space group of C2/c (no. 227). Zhang et al. [13] reported the crystal structure of $CaFeSi_2O_6$ with experimental values are a = 9.8107 Å, b = 8.9856 Å, c = 5.2245 Å, $\alpha = \gamma = 90°$ and $\beta = 104.593°$. The crystal structure consists of corner sharing FeO_6 octahedral and SiO_4 tetrahedral units as shown in Figure 1. To validate the Buckingham potentials (Table S1 in the supplementary information) used in the classical simulation and PAW potentials used in the DFT simulation, energy mimisation calculations were performed and the calculated lattice parameters were compared with corresponding experimental values. The theoretical method reproduced the experimetal structure with the error margin being less than 2% (refer to Table 1).
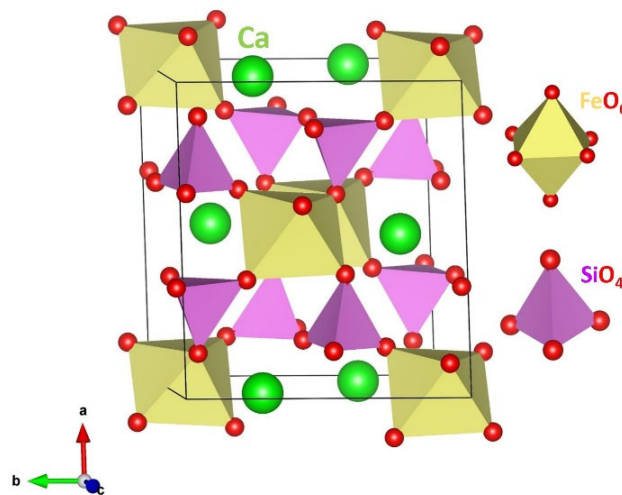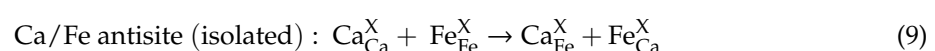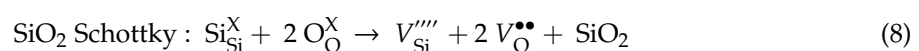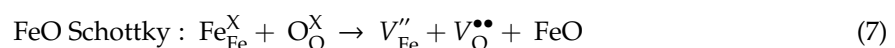
Figure 1. Crystal structure of monoclinic-CaFeSi$_2$O$_6$.

Table 1. Calculate and experimental structural parameters of monoclinic CaFeSi$_2$O$_6$.

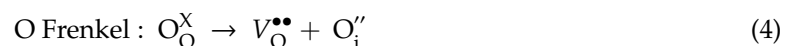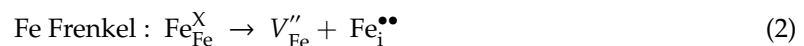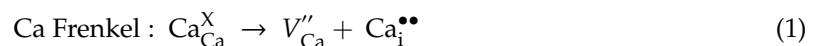| Parameter	Calculated		Experiment [13]	|Δ|(%)	
	Force Field	**DFT**		**Force Field**	**DFT**
a (Å)	9.8716	9.9900	9.8107	0.62	1.83
b (Å)	8.9569	8.9373	8.9856	0.32	0.54
c (Å)	5.2459	5.2256	5.2245	0.41	0.02
α = γ (°)	90.00	90.00	90.00	0.00	0.00
β (°)	105.16	104.01	104.59	0.54	0.56
V (Å^3)	447.7095	452.6849	445.7081	0.45	1.56

3.2. Intrinsic Defect Processes

Point defects in materials are important as they control many physical properties of solids, including diffusion properties and thermodynamic properties. Classical simulations were used to calculate two principle intrinsic point defect energies (vacancies and interstitials). To calculate the Schottky and Frenkel defect processes, energies of point defects were then combined. Anti-site defect in which cations exchange their atomic positons were also calculated. Fourteen intrinsic defect processes were identified, as outlined in Equations (1)–(14) using the Kröger-Vink notation [39].
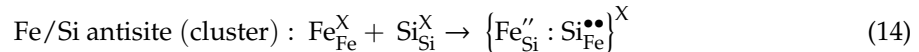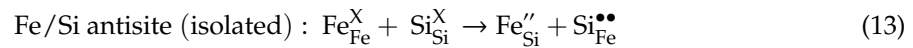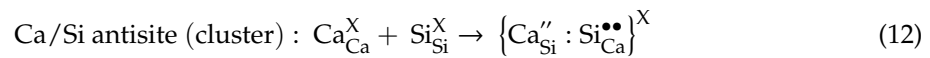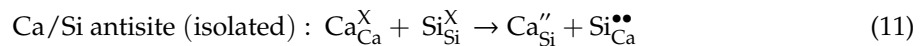
$$\text{Ca Frenkel}: \text{Ca}_{\text{Ca}}^{\text{X}} \rightarrow V_{\text{Ca}}'' + \text{Ca}_{\text{i}}^{\bullet\bullet} \tag{1}$$

$$\text{Fe Frenkel}: \text{Fe}_{\text{Fe}}^{\text{X}} \rightarrow V_{\text{Fe}}'' + \text{Fe}_{\text{i}}^{\bullet\bullet} \tag{2}$$

$$\text{Si Frenkel}: V_{\text{Si}}^{\text{X}} \rightarrow V_{\text{Si}}'''' + \text{Si}_{\text{i}}^{\bullet\bullet\bullet\bullet} \tag{3}$$

$$\text{O Frenkel}: \text{O}_{\text{O}}^{\text{X}} \rightarrow V_{\text{O}}^{\bullet\bullet} + \text{O}_{\text{i}}'' \tag{4}$$

$$\text{Schottky}: \text{Ca}_{\text{Ca}}^{\text{X}} + \text{Fe}_{\text{Fe}}^{\text{X}} + 2\,\text{Si}_{\text{Si}}^{\text{X}} + 6\,\text{O}_{\text{O}}^{\text{X}} \rightarrow V_{\text{Ca}}'' + V_{\text{Fe}}'' + 2\,V_{\text{Si}}'''' + 6\,V_{\text{O}}^{\bullet\bullet} + \text{CaFeSi}_2\text{O}_6 \tag{5}$$

$$\text{CaO Schottky}: \text{Ca}_{\text{Ca}}^{\text{X}} + \text{O}_{\text{O}}^{\text{X}} \rightarrow V_{\text{Ca}}'' + V_{\text{O}}^{\bullet\bullet} + \text{CaO} \tag{6}$$

$$\text{FeO Schottky}: \text{Fe}_{\text{Fe}}^{\text{X}} + \text{O}_{\text{O}}^{\text{X}} \rightarrow V_{\text{Fe}}'' + V_{\text{O}}^{\bullet\bullet} + \text{FeO} \tag{7}$$

$$\text{SiO}_2 \text{ Schottky}: \text{Si}_{\text{Si}}^{\text{X}} + 2\,\text{O}_{\text{O}}^{\text{X}} \rightarrow V_{\text{Si}}'''' + 2\,V_{\text{O}}^{\bullet\bullet} + \text{SiO}_2 \tag{8}$$

$$\text{Ca/Fe antisite (isolated)}: \text{Ca}_{\text{Ca}}^{\text{X}} + \text{Fe}_{\text{Fe}}^{\text{X}} \rightarrow \text{Ca}_{\text{Fe}}^{\text{X}} + \text{Fe}_{\text{Ca}}^{\text{X}} \tag{9}$$

$$Ca/Fe \text{ antisite (cluster)}: Ca_{Ca}^{X} + Fe_{Fe}^{X} \rightarrow \left\{ Ca_{Fe}^{X} : Fe_{Ca}^{X} \right\}^{X} \tag{10}$$

$$Ca/Si \text{ antisite (isolated)}: Ca_{Ca}^{X} + Si_{Si}^{X} \rightarrow Ca_{Si}'' + Si_{Ca}^{\bullet\bullet} \tag{11}$$

$$Ca/Si \text{ antisite (cluster)}: Ca_{Ca}^{X} + Si_{Si}^{X} \rightarrow \left\{ Ca_{Si}'' : Si_{Ca}^{\bullet\bullet} \right\}^{X} \tag{12}$$

$$Fe/Si \text{ antisite (isolated)}: Fe_{Fe}^{X} + Si_{Si}^{X} \rightarrow Fe_{Si}'' + Si_{Fe}^{\bullet\bullet} \tag{13}$$

$$Fe/Si \text{ antisite (cluster)}: Fe_{Fe}^{X} + Si_{Si}^{X} \rightarrow \left\{ Fe_{Si}'' : Si_{Fe}^{\bullet\bullet} \right\}^{X} \tag{14}$$
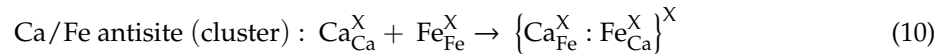
Table 2 reports the defect energies of Frenkel, Schottky and anti-site defect processes. The lowest formation energy is calculated for the Ca-Fe anti-site defect (0.42 eV/defect). This is due to the same charge (+2) of both Ca and Fe. Other anti-site defects (Ca-Fe and Ca-Si) are slightly high due to the charge mismatch. Anti-site defects are common in many oxide materials and have been observed experimentally and theoretically [40–43]. The O Frenkel (2.87 eV/defect) and CaO Schottky (2.97 eV/defect) energies are close to each other and their energies are lower than the other Frenkel or Schottky energies. However, those defects are not significant at normal temperatures. Both Ca and Fe Frenkel energies are ~4.90 eV, suggesting that their formation is unlikely to occur at room temperature. Si Frenkel energy is 9.18 eV/defect inferring the absence of this defect at any conditions.

Table 2. Defect formation energies of intrinsic defect process calculated in monoclinic $CaFeSi_2O_6$.

Defect Process	Equation Number	Defect Energy (eV)	Defect Energy (eV)/Defect
Ca Frenkel	1	9.92	4.96
Fe Frenkel	2	9.74	4.87
Si Frenkel	3	18.36	9.18
O Frenkel	4	5.74	2.87
Schottky	5	38.40	3.84
CaO Schottky	6	5.94	2.97
FeO Schottky	7	6.72	3.36
SiO_2 Schottky	8	14.28	4.76
Ca-Fe anti-site (isolated)	9	0.90	0.45
Ca-Fe anti-site (cluster)	10	0.86	0.42
Ca-Si anti-site (isolated)	11	9.06	4.53
Ca-Si anti-site (cluster)	12	5.26	2.63
Fe-Si anti-site (isolated)	13	5.98	2.98
Fe-Si anti-site (cluster)	14	2.84	1.42

3.3. Calcium Ion Diffusion

To examine the Ca-ion diffusion pathways and their corresponding activation energies, classical simulationes were performed. For a potential high-rate electrode material, ion diffusion with low activation energy of migration is an important factor. The experimental observation of diffusion pathways and their energetics is challenging. In that respect, computational modelling has been useful in providing valuable information on migration pathways and their activation energies [44–48]. We identified two Ca local hops (A and B), as shown in Figure 2. Table 3 reports the Ca-Ca distances and activation energies. In Figure 3, energy profile diagrams for each local hops are shown.

Table 3. Ca local hop distances and their activation energies as shown in Figure 3.

Migration Path	Ca-Ca Separation (Å)	Activation Energy (eV)
A	4.47	4.36
B	5.02	4.49

Calculations show that activation energies are high for both local hops inferring slow diffusion of Ca ions in this material. To construct long-range diffusion pathways, local Ca hops were connected. Two different long-range pathways were identified. The first pathway (A→A→A→A) exhibits a zig-zag pattern in the *bc* plane with overall activation energy of 4.36 eV. The second pathway consists of local hops B (B→B→B→B) and Ca ions migrate in the *ab* plane with overall activation energy of 4.49 eV. High activation energies reveal that very slow Ca-ion diffusion would be expected in $CaFeSi_2O_6$. Table 4 reports the activation energies calculated in previous DFT modelling in different Ca-based electrode materials [11,12]. In general, high activation energy is noted. $CaMn(SiO_3)_2$ exhibits a very high activation energy. This should be due to the long Ca-Ca distances. Notably, both $CaFeSi_2O_6$ and $CaMn(SiO_3)_2$ have the same crystal structures. Both classical and DFT modelling methods provide similar activation energies for these types of materials.
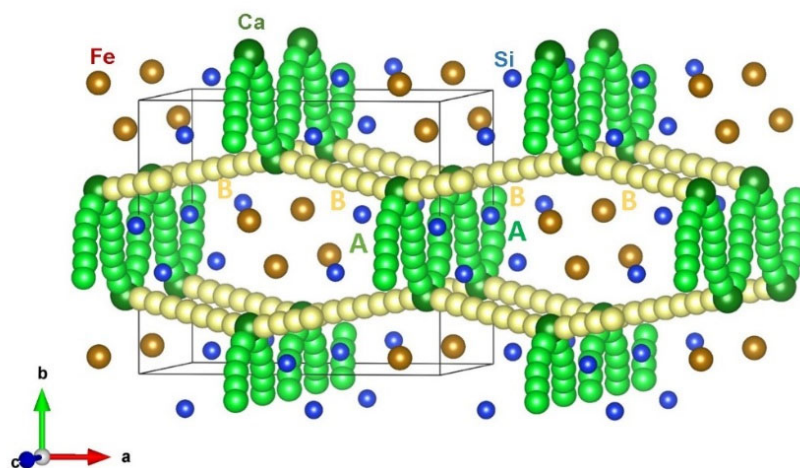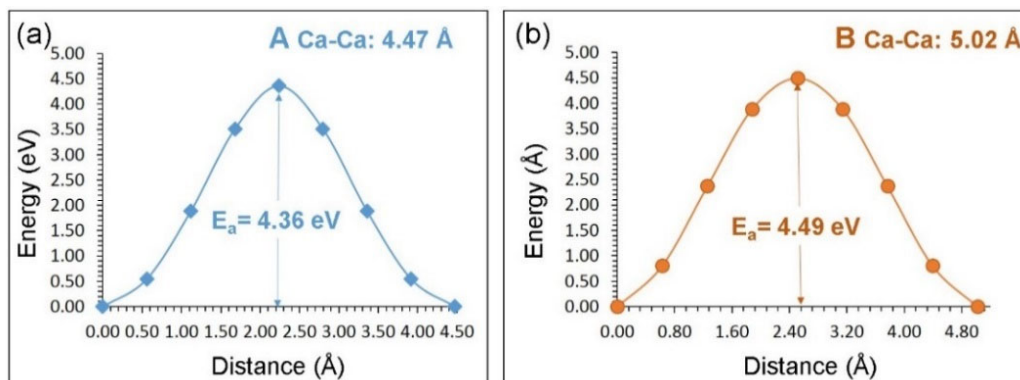

Figure 2. Calculated long-range calcium ion diffusion pathways. Yellow- and green-coloured atoms show two different Ca trajectories.

Figure 3. Energy profiles diagrams for local Ca hops (**a**) A and (**b**) B as shown in Figure 2.

Table 4. Activation energy calculated for Ca-ion migration in Ca-based electrode materials.

Material	Activation Energy (eV)
$CaMn(SiO_3)_2$	4.60 [11]
$Ca_3Cr_2(SiO_4)_3$	2.07 [11]
$Ca_3Mn_2(SiO_4)_3$	2.09 [11]
$Ca_{11}Mn_{12}C_{24}O_{72}$	2.80 [11]
$CaMn_2O_4$	1.00 [12]

3.4. Solution of Dopants

Performance of an electrode material can be improved by doping aliovalent or isovalent dopants via introducing charge compensating point defects (vacancies and interstitials) in the lattice. Here we investigated the substitution of a range of dopant ions in $CaFeSi_2O_6$ using classical simulation to test the most favourable dopants experimentally.

3.4.1. Divalent Dopants

Both Ca and Fe sites were considered for substituion with some divalent cations (M = Ni, Mg, Co, Zn, Mn, Sr and Ba) and the following reaction equations were used to calculate reaction enthalpies. Substitution of divalent cations at the divalent cation sites in the lattice does not require another defect for charge compensation.

$$MO + Ca_{Ca}^X \rightarrow M_{Ca}^X + CaO \tag{15}$$

$$MO + Fe_{Fe}^X \rightarrow M_{Fe}^X + FeO \tag{16}$$

Figure 4 reports the solution enthalpy as a function of the radius of the dopant ion. The lowest solution enthalpy (0.01 eV) is calculated for Sr^{2+} ion at the Ca site (refer to Figure 4a). The ionic radius of Ca^{2+} is 1.00 Å. The preference of Sr^{2+} can be due to position of both Ca^{2+} and Sr^{2+} ions in the same group. The second favourable dopant is Mn^{2+} with the soultion enthalpy of 0.56 eV and its ionic radius (0.96 Å) is very close to that of Ca^{2+} (1.00 Å). Solution enthalpy decreases with the increase of ionic radius from Ni^{2+} to Sr^{2+}. This is mainly due to the decrease in the cation mismatch. The soution enthalpy of Ba^{2+} is 1.03 eV due to its larger ionic radius than that of Ca^{2+}.

Exoergic solution enthalpy is calculated for Mn^{2+} at the Fe site. The ionic radius of Fe^{2+} in an octahedral environment is 0.61 Å. Solution enthalpies for Co^{2+}, Ni^{2+}, Mg^{2+} and Zn^{2+} are very small and range between 0.02 eV and 0.10 eV meaning that they are also candidate dopants. Both Sr^{2+} and Ba^{2+} exhibit high solution enthalpies.This is beacause of their larger ionic radii than that of Fe^{2+} ion.
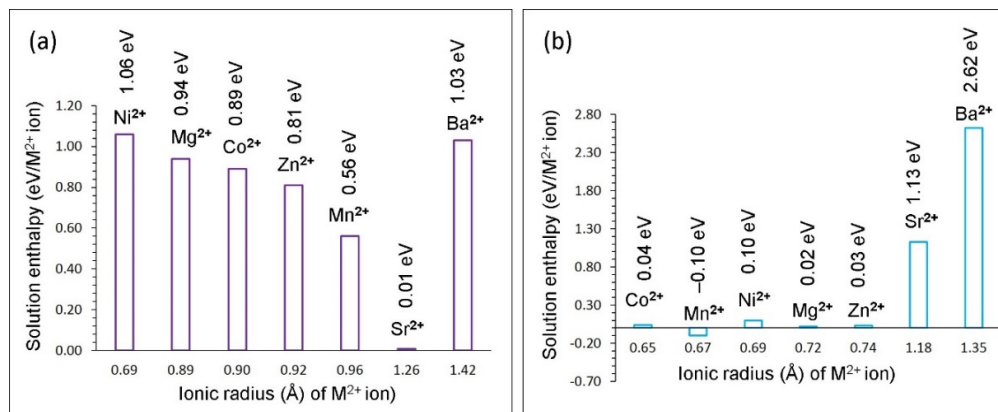

Figure 4. Solution enthalpies caclulated for MO (M = Ni, Mg, Co, Zn, Mn and Sr) at the (**a**) Ca and (**b**) Fe sites with respect to the M^{2+} ionic radius.

3.4.2. Trivalent Dopants

Additional Ca^{2+} ions can improve its capacity and then enhance ionic conductivity in $CaFeSi_2O_6$. Here we suggest a stratergy to form Ca interstitials by doping trivalent cations (Al, Sc, In, Y, Gd, La and Ga) at the Si site. Previous modelling studies also considered the same strategy in different battery materials and validity of this stratergy has been confirmed by experimental studies in Li_2RuO_3 [49]. The solution of M_2O_3 (R = Al, Sc, In, Y, Gd, La and Ga) was considered using the following reaction (in Kröger-Vink notation).

$$M_2O_3 + 2Si_{Si}^X + CaO \rightarrow 2\,M'_{Si} + 2\,Ca_i^{\bullet\bullet} + 2\,SiO_2 \tag{17}$$
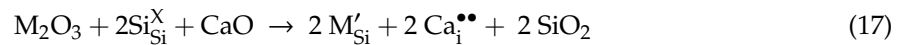
Figure 5a reports the solution enthalpies of M_2O_3. The current simulations show that the most favourable dopant is the Al^{3+} but the solution enthalpy is highly endothermic. This indicates that the additional Ca can be formed in the form of interstitials into $CaFeSi_2O_6$. Experimental verification is needed to determine the exact concentration of the composition. The possible structure of doped compound can be written as $CaFeSi_{2-x}Al_xO_6$ (x = 0.0–1.0).

Doping of trivalent dopants at the Fe site can facilitate the formation of Ca vacancies required for the vacancy assisted Ca diffusion and CaO Schottky formation. Figure 5b reports the solution enthalpies calculated using the following reaction equation.

$$M_2O_3 + 2Fe_{Fe}^X + Ca_{Ca}^X \rightarrow 2\,M_{Fe}^{\bullet} + V''_{Ca} + CaO + 2FeO \tag{18}$$
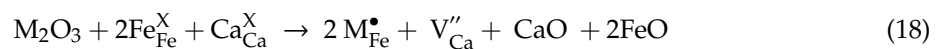
In all cases, solution enthalpies are endothermic, suggesting that a high temperature is required for this process. Current calculations were performed at 0 K and it is anticipated that at high temperature, solution enthalpy values would be less positive. A favourable dopant in this process is Ga. This could be due to the very small difference between ionic radii of Ga^{3+} (0.62 Å) and Fe^{2+} (0.61 Å). The highest solution enthalpy is calculated for Al^{3+}. Both Sc and In exhibit almost similar solution enthalpies deviating only by ~0.08 eV from the value calculated for Ga^{3+}. From Y to La, solution enthalpies increase gradually with ionic radius.
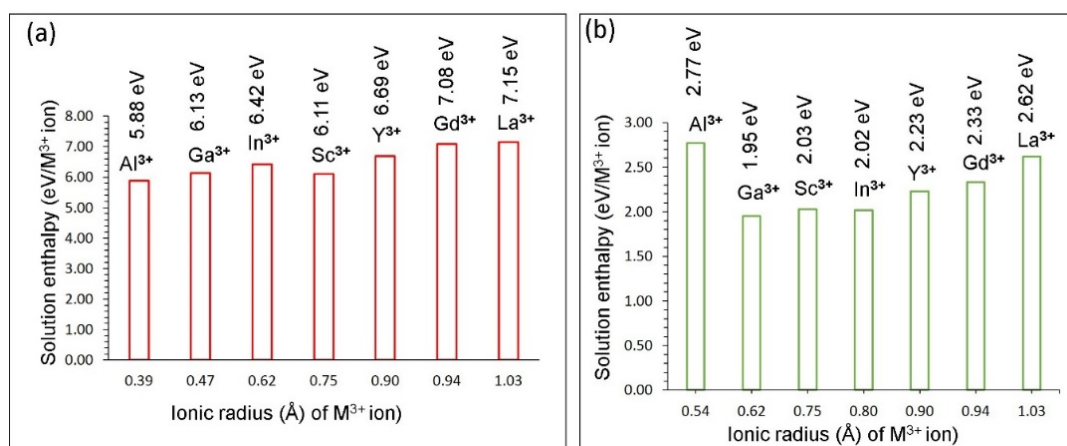

Figure 5. Solution enthalpies caclulated for M_2O_3 (M = Al, Ga, In, Sc, Y, Gd and La) at the Fe site with the formation of (**a**) Ca interstitials and (**b**) Ca vacancies with respect to the M^{3+} ionic radius.

Here we calculate the activation energies for Ca-ion diffusion in the presence of Al^{3+} on the Si site. Figure 6 shows the energy profile diagrams for the local Ca hops.
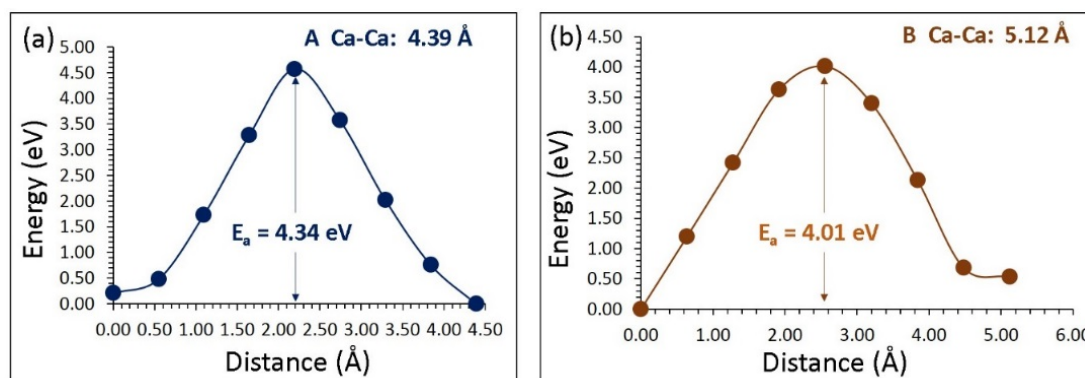
Figure 6. Energy profile diagrams for the Ca local hops (**a**) A and (**b**) B in the presence of Al on the Si site (refer to Figure 2).

There is a slight reduction (by 0.02 eV) in the activation energy for the local hop A. In the case of hop B, activation energy is reduced by 0.48 eV. In both cases, Ca-Ca distances have been elongated compared to the distances present in the pure crystal structure. This perturbation in the distances can be due to the charge and ionic radius mismatch between Al^{3+} and Si^{4+}. Our simulation predicts that doping Al on the Si site would not only increase the concentration of Ca^{2+} ions in the lattice but also reduces the activation energy of the Ca-ion migration.

3.4.3. Tetravalent Dopants

Here we discuss the results obtained from doping of some tetravalent dopants (Ge^{4+}, Ti^{4+}, Sn^{4+}, Zr^{4+} and Ce^{4+}) at the Si site. Solution enthalpy was calculated using the following reaction equation.

$$MO_2 + Si_{Si}^X \rightarrow M_{Si}^X + SiO_2 \qquad (19)$$

Promising dopant for this process is Ge with the lowest solution enthalpy of 0.65 eV (see Figure 7). This is because of the fact that ionic radii of both Ge^{4+} (0.39 Å) and Si^{4+} (0.40 Å) are very close. Solution enthalpy for the doping of Ti^{4+} is 3.20 eV higher by ~2.50 eV than that calculated for Ge^{4+}. Solution enthalpy increases with ionic radius from Sn to Ce. Solution enthalpy for CeO_2 is 4.19 eV meaning that this highly endoergic process mainly occurs at high temperatures.
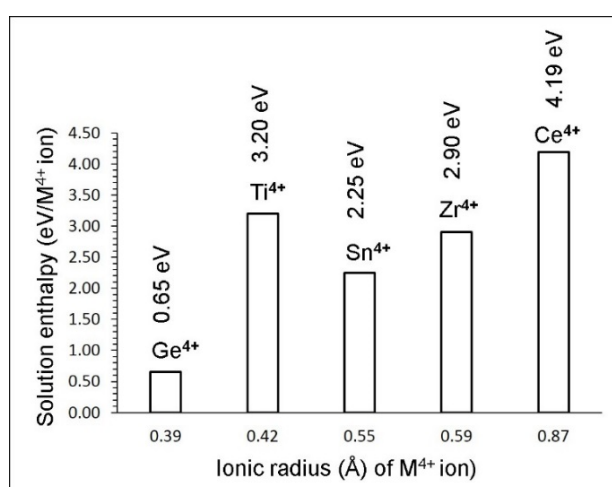

Figure 7. Solution enthalpies calculated for tetravalent dopants at the Si site with respect to dopant ionic radius.

3.5. Electronic Structures of Doped CaFeSi$_2$O$_6$

We employed DFT to examine the electronic structures of defect free and doped-CaFeSi$_2$O$_6$ configurations. The promising dopants were only considered as discussed in the previous sections.

Previous DFT simulations by Streltsov et al. [50] discussed the electronic structure of CaFeSi$_2$O$_6$. Their calculation show that CaFeSi$_2$O$_6$ is a wide gap semiconductor with the band gap of 3.80 eV which is in agreement with the calculated band gap of 3.40 eV in this study (see Figure 8c). Furthermore, the total DOS (density of states) plot shows that there should be a net magnetic moment present as spin-up and spin-down states are not symmetric.

First we considered the electronic structure of Sr substituted at the Ca site in CaFeSi$_2$O$_6$. The Sr-O bond distances are slightly longer than the Ca-O bond distances. This is due to the larger ionic radius of Sr^{2+} (1.26 Å) than that of Ca^{2+} (1.00 Å). Fermi energy and band gap were almost unaltered with the doping of Sr (see Figure 8d). However, the states occupied in the gap region sligltly perturbes. Atomic DOS of Sr is shown in Figure 8e.
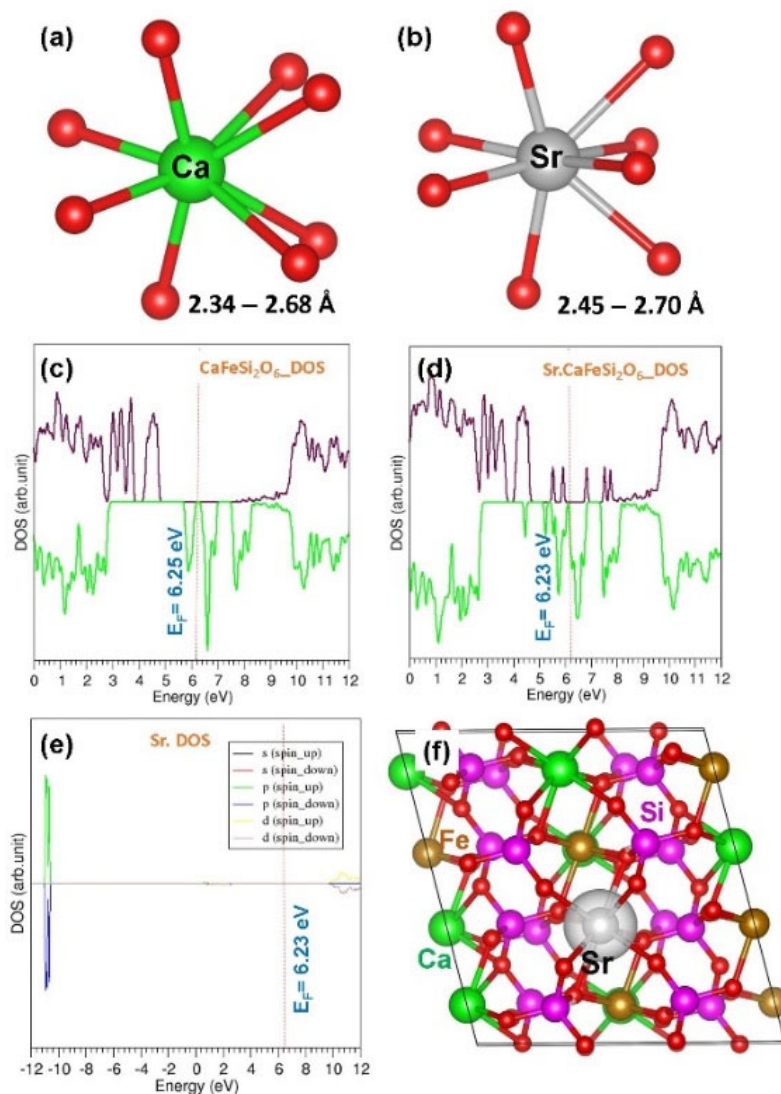

Figure 8. (**a**,**b**) Distorted CaO$_8$ and SrO$_8$ units showing bond lengths in defect free and defect (Sr-doped) configurations respectively, (**c**,**d**) corresponding total DOSs (**e**) atomic DOS of Sr and (**f**) constant charge density around the dopant.

Next we discuss the electronic structure of Mn substituted at the Fe site. Calculated Fe-O and Mn-O bond distances are almost the same. This is due to the similar ionic radius of Fe^{2+} (0.61 Å) and Mn^{2+} (0.67 Å). Doping of Mn reduces the Fermi energy slightly (by 0.05 eV) and band gap significantly (by 0.80 eV) (see Figure 9).
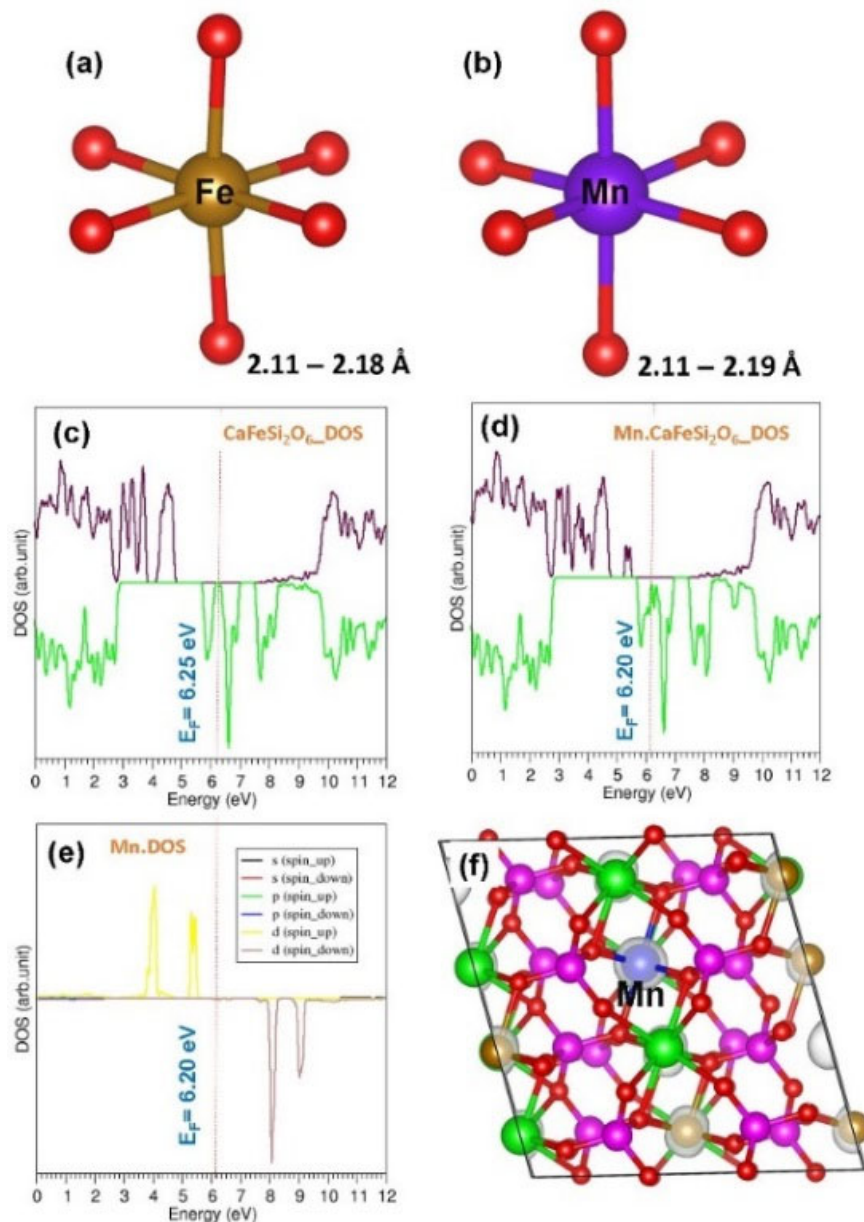

Figure 9. (**a,b**) Distorted FeO_6 and MnO_6 octahedral units showing bond lengths in defect free and defect (Mn-doped) configurations respectively, (**c,d**) corresponding total DOSs (**e**) atomic DOS of Mn and (**f**) constant charge density around the dopant.

Doping of Al at the Si site was next considered. Al-O bond distances are slightly longer than Si-O bond distances (see Figure 10). This is due to the larger ionic radius of Al^{3+} than that of Si^{4+} in a tetrahedral coordination. Fermi energy is shifted by 0.21 eV upon doping. Fermi energy level is occupied by additional states mainly arising from p states of Al (see Figure 10d,e). Substitution of Al at the Si site introduces an electron in the lattice and makes the resultant compound metallic.
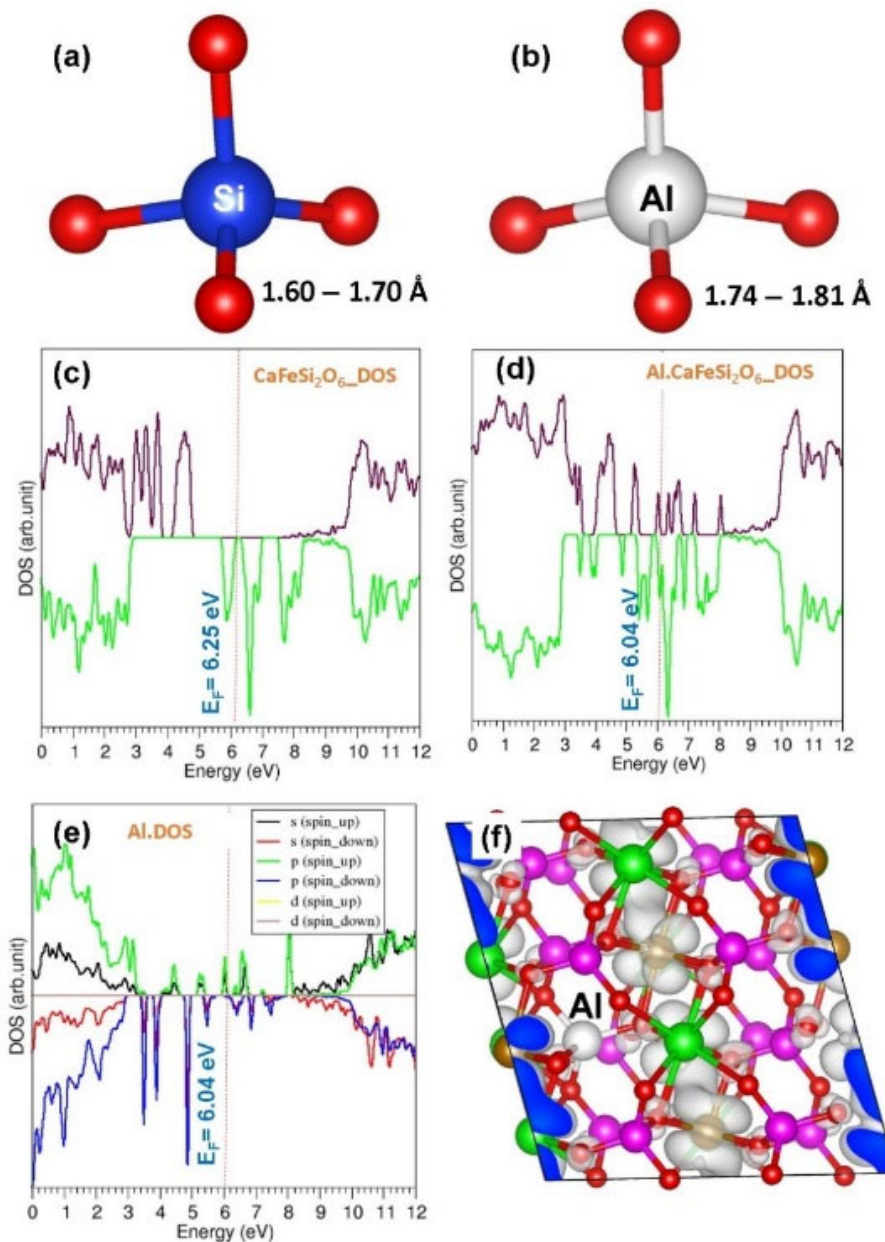
Figure 10. (**a**,**b**) Distorted SiO_4 and AlO_4 octahedral units showing bond lengths in defect free and defect (Al-doped) configurations respectively, (**c**,**d**) corresponding total DOSs (**e**) atomic DOS of Al and (**f**) constant charge density around the dopant.

Calculated bond lengths show that Fe-O bond distances are shorter than the Ga-O bond distances. Ionic radii of both Fe^{2+} and Ga^{3+} ions are close to each other. However, charge density of Ga^{3+} is greater than that of Fe^{2+} due to the higher charge (+3) of Ga than that of Fe (+2). Shorter Ga-O bond distances are due to the strong ionic interaction between Ga^{3+} and O^{2-}. Fermi energy increase by 0.35 eV upon Ga doping (see Figure 11). There are no significant peaks arising from Ga near Fermi energy level or in the gap according to the atomic DOS of Ga. However, there is a significant reorientation of spin states and the resultant doped configuration exhibits metallic character.
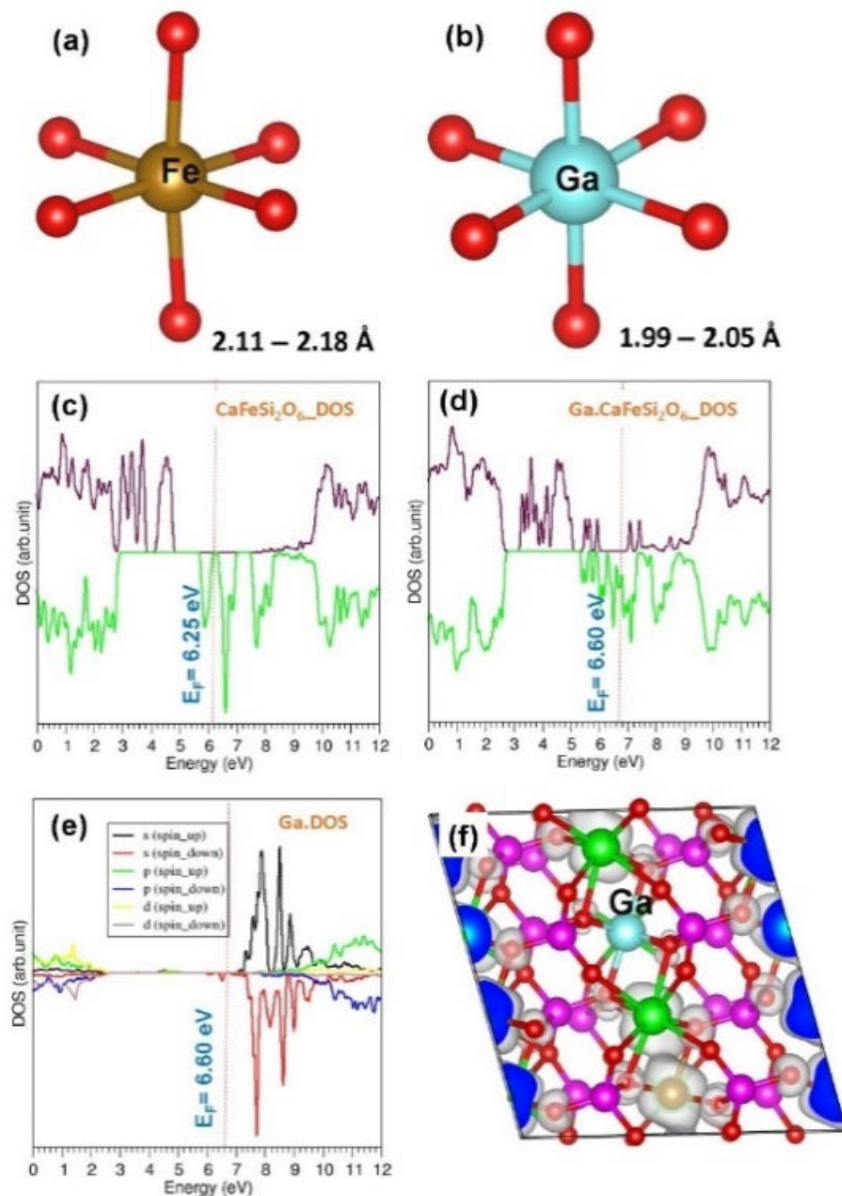
Figure 11. (**a**,**b**) Distorted FeO_6 and GaO_6 octahedral units showing bond lengths in defect free and defect (Ga-doped) configurations respectively, (**c**,**d**) corresponding total DOSs (**e**) atomic DOS of Ga and (**f**) constant charge density around the dopant.

Finally, Ge was introduced at the Si site. Though Ge and Si are isovalent atoms, their ionic radii are different (Si^{4+}: 0.26 Å and Ge^{4+}: 0.39 Å). Larger ionic radius of Ge^{4+} reflects in the longer Ge-O bond distances (see Figure 12). Total DOS plot of Ge-doped $CaFeSi_2O_6$ is almost unaltered near the Fermi level. This is further confirmed by the atomic DOS of Ge. The Fermi energy is lowered only by 0.08 eV upon Ge substitution. Charge density plot shows that there is a slight perturbation of electron charge density around Fe atoms only. However, charge localization is not observed around the Ge due to the isoelectronic nature of both Si and Ge.
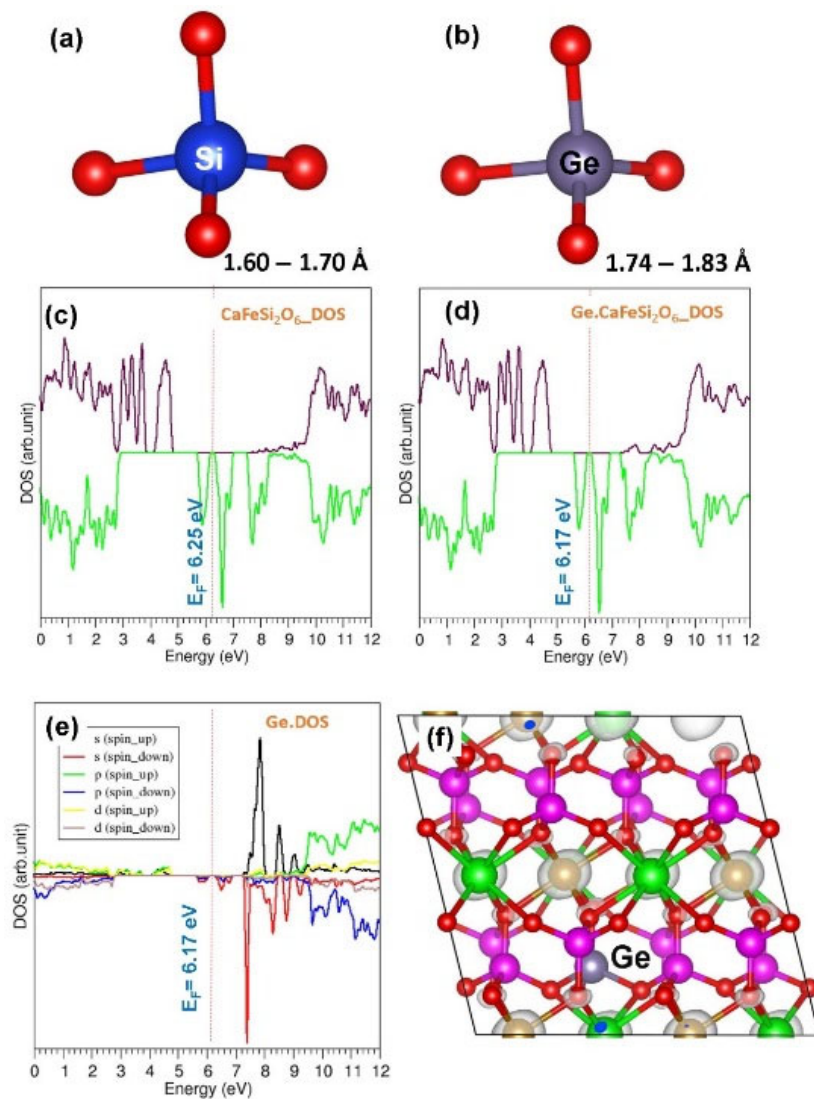
Figure 12. (**a**,**b**) Distorted SiO_4 and GeO_4 tetrahedral units showing bond lengths in defect free and defect (Ge-doped) configurations respectively, (**c**,**d**) corresponding total DOSs (**e**) atomic DOS of Ge and (**f**) constant charge density around the dopant.

4. Conclusions

We used computational techniques to provide a detailed atomistic level understanding of key defect processes, diffusion mechanisms and dopant properties in $CaFeSi_2O_6$. Calculations show that the Ca-Fe anti-site defect would be dominant in this material. The formation of Frenkel defects is unlikely under normal conditions though the O Frenkel exhibits the lowest Frenkel energy of 2.87 eV/defect. The loss of CaO in this material requires a moderate temperature and can be facilitated by introducing additional Ca vacancies. Ca-ion diffusion in this material is found to be very slow. Doping of Al at the Si site is anticipated to improve the capacity and ion diffusion. Formation of Ca vacancies required for the CaO Schottky can be facilitated by doping Ga at the Fe site. Electronic structure calculations show that $CaFeSi_2O_6$ is a wide-gap semiconductor. While isovalent dopants do not affect the electronic structure much, aliovalent dopants alter the electronic structure and gap states.

Author Contributions: Computation, N.K.; Writing, N.K.; Analysis and Editing, A.C. All authors have read and agreed to the published version of the manuscript.

Conflicts of Interest: The authors declare no conflict of interest.

References

1.　Liu, Y.; Zhou, Y.; Zhang, J.; Xia, Y.; Chen, T.; Zhang, S. Monoclinic Phase $Na_3Fe_2(PO_4)_3$: Synthesis, Structure, and Electrochemical Performance as Cathode Material in Sodium-Ion Batteries. *ACS Sustain. Chem. Eng.* **2017**, *5*, 1306–1314. [CrossRef]

2.　Yabuuchi, N.; Kubota, K.; Dahbi, M.; Komaba, S. Research Development on Sodium-Ion Batteries. *Chem. Rev.* **2014**, *114*, 11636–11682. [CrossRef] [PubMed]

3.　Hwang, J.-Y.; Myung, S.-T.; Sun, Y.-K. Sodium-ion batteries: Present and future. *Chem. Soc. Rev.* **2017**, *46*, 3529–3614. [CrossRef] [PubMed]

4.　Kim, J.; Yoon, G.; Kim, H.; Park, Y.-U.; Kang, K. $Na_3V(PO_4)_2$: A New Layered-Type Cathode Material with High Water Stability and Power Capability for Na-Ion Batteries. *Chem. Mater.* **2018**, *30*, 3683–3689. [CrossRef]

5.　Xu, C.; Li, B.; Du, H.; Kang, F. Energetic Zinc Ion Chemistry: The Rechargeable Zinc Ion Battery. *Angew. Chem. Int. Ed.* **2012**, *51*, 933–935. [CrossRef]

6.　Muldoon, J.; Bucur, C.B.; Gregory, T. Quest for Nonaqueous Multivalent Secondary Batteries: Magnesium and Beyond. *Chem. Rev.* **2014**, *114*, 11683–11720. [CrossRef] [PubMed]

7.　Ponrouch, A.; Frontera, C.; Bardé, F.; Palacín, M.R. Towards a calcium-based rechargeable battery. *Nat. Mater.* **2015**, *15*, 169–172. [CrossRef]

8.　Novák, P.; Imhof, R.; Haas, O. Magnesium insertion electrodes for rechargeable nonaqueous batteries—A competitive alternative to lithium? *Electrochim. Acta* **1999**, *45*, 351–367. [CrossRef]

9.　Aurbach, D.; Gofer, Y.; Lu, Z.; Schechter, A.; Chusid, O.; Gizbar, H.; Cohen, Y.; Ashkenazi, V.; Moshkovich, M.; Turgeman, R.; et al. A short review on the comparison between Li battery systems and rechargeable magnesium battery technology. *J. Power Sources* **2001**, *97*, 28–32. [CrossRef]

10.　Gummow, R.J.; Vamvounis, G.; Kannan, M.B.; He, Y. Calcium-Ion Batteries: Current State-of-the-Art and Future Perspectives. *Adv. Mater.* **2018**, *30*, 1801702. [CrossRef]

11.　Torres, A.; Luque, F.J.; Tortajada, J.; Arroyo-de Dompablo, M.E. Analysis of Minerals as Electrode Materials for Ca-based Rechargeable Batteries. *Sci. Rep.* **2019**, *9*, 9644. [CrossRef] [PubMed]

12.　Dompablo, M.E.A.-d.; Krich, C.; Nava-Avendaño, J.; Biškup, N.; Palacín, M.R.; Bardé, F. A Joint Computational and Experimental Evaluation of $CaMn_2O_4$ Polymorphs as Cathode Materials for Ca Ion Batteries. *Chem. Mater.* **2016**, *28*, 6886–6893. [CrossRef]

13.　Zhang, L.; Ahsbahs, H.; Hafner, S.S.; Kutoglu, A. Single-crystal compression and crystal structure of clinopyroxene up to 10 GPa. *Am. Mineral.* **1997**, *82*, 245–258. [CrossRef]

14.　Nishimura, S.-I.; Hayase, S.; Kanno, R.; Yashima, M.; Nakayama, N.; Yamada, A. Structure of Li_2FeSiO_4. *J. Am. Chem. Soc.* **2008**, *130*, 13212–13213. [CrossRef] [PubMed]

15.　Law, M.; Ramar, V.; Balaya, P. Na_2MnSiO_4 as an attractive high capacity cathode material for sodium-ion battery. *J. Power Sources* **2017**, *359*, 277–284. [CrossRef]

16.　Redfern, S.A.T.; Artioli, G.; Rinaldi, R.; Henderson, C.M.B.; Knight, K.S.; Wood, B.J. Octahedral cation ordering in olivine at high temperature. II: An in situ neutron powder diffraction study on synthetic $MgFeSiO_4$ (Fa50). *Phys. Chem. Miner.* **2000**, *27*, 630–637. [CrossRef]

17.　Kuganathan, N.; Islam, M.S. Li_2MnSiO_4 Lithium Battery Material: Atomic-Scale Study of Defects, Lithium Mobility, and Trivalent Dopants. *Chem. Mater.* **2009**, *21*, 5196–5202. [CrossRef]

18.　Kuganathan, N.; Chroneos, A. Defects, Dopants and Sodium Mobility in Na_2MnSiO_4. *Sci. Rep.* **2018**, *8*, 14669. [CrossRef]

19.　Armstrong, A.R.; Kuganathan, N.; Islam, M.S.; Bruce, P.G. Structure and Lithium Transport Pathways in Li_2FeSiO_4 Cathodes for Lithium Batteries. *J. Am. Chem. Soc.* **2011**, *133*, 13031–13035. [CrossRef]

20.　Liivat, A.; Thomas, J.O. Li-ion migration in Li_2FeSiO_4-related cathode materials: A DFT study. *Solid State Ion.* **2011**, *192*, 58–64. [CrossRef]

21.　Rupasov, D.; Chroneos, A.; Parfitt, D.; Kilner, J.A.; Grimes, R.W.; Istomin, S.Y.; Antipov, E.V. Oxygen diffusion in $Sr_{0.75}Y_{0.25}CoO_{2.625}$: A molecular dynamics study. *Phys. Rev. B* **2009**, *79*, 172102. [CrossRef]

22. Grimes, R.W.; Busker, G.; McCoy, M.A.; Chroneos, A.; Kilner, J.A.; Chen, S.-P. The Effect of Ion Size on Solution Mechanism and Defect Cluster Geometry. *Ber. Der Bunsenges. Für Phys. Chem.* **1997**, *101*, 1204–1210. [CrossRef]

23. Jay, E.E.; Rushton, M.J.D.; Chroneos, A.; Grimes, R.W.; Kilner, J.A. Genetics of superionic conductivity in lithium lanthanum titanates. *Phys. Chem. Chem. Phys.* **2015**, *17*, 178–183. [CrossRef] [PubMed]

24. Kuganathan, N.; Kordatos, A.; Chroneos, A. Li_2SnO_3 as a Cathode Material for Lithium-ion Batteries: Defects, Lithium Ion Diffusion and Dopants. *Sci. Rep.* **2018**, *8*, 12621. [CrossRef]

25. Kuganathan, N.; Chroneos, A. Defects and dopant properties of $Li_3V_2(PO_4)_3$. *Sci. Rep.* **2019**, *9*, 333. [CrossRef]

26. Kuganathan, N.; Chroneos, A. Defect Chemistry and Na-Ion Diffusion in $Na_3Fe_2(PO_4)_3$ Cathode Material. *Materials* **2019**, *12*, 1348. [CrossRef]

27. Gale, J.D. GULP: A computer program for the symmetry-adapted simulation of solids. *J. Chem. Soc. Faraday Trans.* **1997**, *93*, 629–637. [CrossRef]

28. Gale, J.D.; Rohl, A.L. The General Utility Lattice Program (GULP). *Mol. Simul.* **2003**, *29*, 291–341. [CrossRef]

29. Mott, N.F.; Littleton, M.J. Conduction in polar crystals. I. Electrolytic conduction in solid salts. *Trans. Faraday Soc.* **1938**, *34*, 485–499. [CrossRef]

30. Kuganathan, N.; Ganeshalingam, S.; Chroneos, A. Defects, Diffusion, and Dopants in $Li_2Ti_6O_{13}$: Atomistic Simulation Study. *Materials* **2019**, *12*, 2851. [CrossRef]

31. Catlow, C.R.A. *"SolidState Chemistry: Techniques"*; Cheetham, A.K., Day, P., Eds.; Clarendon Press: Oxford, UK, 1987; p. 231.

32. Kresse, G.; Furthmüller, J. Efficient iterative schemes for ab initio total-energy calculations using a plane-wave basis set. *Phys. Rev. B* **1996**, *54*, 11169–11186. [CrossRef] [PubMed]

33. Kresse, G.; Joubert, D. From ultrasoft pseudopotentials to the projector augmented-wave method. *Phys. Rev. B* **1999**, *59*, 1758–1775. [CrossRef]

34. Blöchl, P.E. Projector augmented-wave method. *Phys. Rev. B* **1994**, *50*, 17953–17979. [CrossRef] [PubMed]

35. Monkhorst, H.J.; Pack, J.D. Special points for Brillouin-zone integrations. *Phys. Rev. B* **1976**, *13*, 5188–5192. [CrossRef]

36. Perdew, J.P.; Burke, K.; Ernzerhof, M. Generalized Gradient Approximation Made Simple. *Phys. Rev. Lett.* **1996**, *77*, 3865–3868. [CrossRef] [PubMed]

37. Press, W.H.; Teukolsky, S.A.; Vetterling, W.T.; Flannery, B.P. *Numerical Recipes in C The Art of Scientific Computing*, 2nd ed.; Cambridge University Press: Cambridge, UK, 1992; p. 994.

38. Grimme, S.; Antony, J.; Ehrlich, S.; Krieg, H. A consistent and accurate ab initio parametrization of density functional dispersion correction (DFT-D) for the 94 elements H-Pu. *J. Chem. Phys.* **2010**, *132*, 154104. [CrossRef]

39. Kröger, F.A.; Vink, H.J. Relations between the Concentrations of Imperfections in Crystalline Solids. In *Solid State Physics*; Seitz, F., Turnbull, D., Eds.; Academic Press: New York, NY, USA, 1956; Volume 3, pp. 307–435.

40. Ensling, D.; Stjerndahl, M.; Nytén, A.; Gustafsson, T.; Thomas, J.O. A comparative XPS surface study of Li_2FeSiO_4/C cycled with LiTFSI- and $LiPF_6$-based electrolytes. *J. Mater. Chem.* **2009**, *19*, 82–88. [CrossRef]

41. Liu, H.; Choe, M.-J.; Enrique, R.A.; Orvañanos, B.; Zhou, L.; Liu, T.; Thornton, K.; Grey, C.P. Effects of Antisite Defects on Li Diffusion in $LiFePO_4$ Revealed by Li Isotope Exchange. *J. Phys. Chem. C* **2017**, *121*, 12025–12036. [CrossRef]

42. Kempaiah Devaraju, M.; Duc Truong, Q.; Hyodo, H.; Sasaki, Y.; Honma, I. Synthesis, characterization and observation of antisite defects in LiNiPO4 nanomaterials. *Sci. Rep.* **2015**, *5*, 11041. [CrossRef]

43. Politaev, V.V.; Petrenko, A.A.; Nalbandyan, V.B.; Medvedev, B.S.; Shvetsova, E.S. Crystal structure, phase relations and electrochemical properties of monoclinic Li_2MnSiO_4. *J. Solid State Chem.* **2007**, *180*, 1045–1050. [CrossRef]

44. Islam, M.S.; Driscoll, D.J.; Fisher, C.A.J.; Slater, P.R. Atomic-Scale Investigation of Defects, Dopants, and Lithium Transport in the $LiFePO_4$ Olivine-Type Battery Material. *Chem. Mater.* **2005**, *17*, 5085–5092. [CrossRef]

45. Fisher, C.A.J.; Hart Prieto, V.M.; Islam, M.S. Lithium Battery Materials LiMPO4 (M = Mn, Fe, Co, and Ni): Insights into Defect Association, Transport Mechanisms, and Doping Behavior. *Chem. Mater.* **2008**, *20*, 5907–5915. [CrossRef]

46. Perera, D.; Ganeshalingam, S.; Kuganathan, N.; Chroneos, A. A Computational Study of Defects, Li-Ion Migration and Dopants in Li_2ZnSiO_4 Polymorphs. *Crystals* **2019**, *9*, 563. [CrossRef]

47. Kaushalya, R.; Iyngaran, P.; Kuganathan, N.; Chroneos, A. Defect, Diffusion and Dopant Properties of $NaNiO_2$: Atomistic Simulation Study. *Energies* **2019**, *12*, 3094. [CrossRef]

48. Kuganathan, N.; Gkanas, E.I.; Chroneos, A. Mg_6MnO_8 as a Magnesium-Ion Battery Material: Defects, Dopants and Mg-Ion Transport. *Energies* **2019**, *12*, 3213. [CrossRef]

49. Kuganathan, N.; Kordatos, A.; Chroneos, A. Defect Chemistry and Li-ion Diffusion in Li_2RuO_3. *Sci. Rep.* **2019**, *9*, 550. [CrossRef]

50. Streltsov, S.; Skorikov, N. Spin-state transitions in $CaFeSi_2O_6$ and $NaFeSi_2O_6$ under pressure. *Phys. Rev. B* **2011**, *83*, 214407. [CrossRef]